



Cite this: *Phys. Chem. Chem. Phys.*,
2015, 17, 12623

Structural phase transformation and microwave dielectric studies of $\text{SmNb}_{1-x}(\text{Si}_{1/2}\text{Mo}_{1/2})_x\text{O}_4$ compounds with fergusonite structure

S. D. Ramarao and V. R. K. Murthy*

Temperature- and composition-induced phase transition in SmNbO_4 was studied by differential scanning calorimetry, Raman spectroscopy and high-temperature powder X-ray diffraction measurements. *In situ* X-ray diffraction studies revealed that SmNbO_4 possesses a monoclinic fergusonite crystal structure at ambient temperature and transforms to a tetragonal scheelite structure above the transition temperature ($T_o \geq 800^\circ\text{C}$). The second-order nature of this transition was confirmed by observing a linear relationship between the spontaneous strain (ϵ_s) of SmNbO_4 and the Landau order parameter (η) around the phase transition temperature. We stabilized this high-temperature tetragonal scheelite phase at ambient temperature by substituting Si^{4+} and Mo^{6+} into the Nb site of SmNbO_4 . The $\text{SmNb}_{1-x}(\text{Si}_{1/2}\text{Mo}_{1/2})_x\text{O}_4$ ($x = 0.0\text{--}0.69$) ceramic compositions were prepared by the conventional solid-state reaction method. Rietveld refinement was carried out on all the compositions to examine the phase purity, and the compositions where $x < 0.06$ all formed a monoclinic fergusonite structure ($I2/a$ space group, $Z = 2$). Both the X-ray diffraction and Raman spectroscopy measurements revealed that increasing the concentration of x transformed the structure from monoclinic fergusonite to tetragonal scheelite ($I4_1/a$ space group, $Z = 4$) at a critical concentration (x_c). Both the monoclinic and tetragonal phases coexisted in the composition range of $0.06 \leq x < x_c$. The Hakki–Coleman and reflection cavity techniques were used to measure the dielectric constant and quality factor of these stabilized phases, respectively. The temperature coefficient of the resonant frequency was measured by using an invar cavity attached to a programmable hot plate. The high-density samples possessed good microwave dielectric properties.

Received 29th January 2015,
Accepted 9th April 2015

DOI: 10.1039/c5cp00569h

www.rsc.org/pccp

1. Introduction

Compounds with ABO_4 stoichiometry are technologically important materials that have a wide variety of interesting applications as scintillators, Cherenkov detectors, acousto-optic devices, and laser host materials. There are numerous studies of ABO_4 materials for cathode materials in solid-state fuel cells, and as photocatalytic and photoluminescent materials.^{1–5} These compounds can accommodate different crystal structures depending on the ionic radii and their ratio, valence (I–VII, II–VI, III–V and IV–IV), coordination number and electronic configuration (filling of d and f shells) of the B-site cation.⁶

Generally, metal orthomolybdate ($\text{A}^{2+}\text{MoO}_4$) and orthotungstate (A^{2+}WO_4) compounds possess a scheelite structure when the A-site is occupied by large bivalent cations (ionic radius $> 0.99 \text{ \AA}$) such as Ca, Ba, Sr, Pb, and Eu. In contrast, $\text{A}^{2+}(\text{Mo}, \text{W})\text{O}_4$ compounds with smaller bivalent cations (ionic radius $< 0.77 \text{ \AA}$, Zn, Co, Ni, Mn and Fe) at the A-site have a wolframite crystal structure.⁶

Recently, research has focused on the microwave dielectric properties of $\text{A}^{2+}\text{B}^{6+}\text{O}_4$ (A: Ca, Sr, Ba, Zn, Ni, Mg; B: Mo, W) ceramic compositions with scheelite and wolframite crystal structures because of the flexibility in substituting different elements at the A- and B-site to obtain optimum microwave dielectric properties.^{7–11}

Ewing reported the crystal chemistry of different classes of material containing niobium and tantalum.¹² However, pure rare-earth orthoniobates (RENbO_4) crystallize in the monoclinic fergusonite crystal structure ($I2/a$, C_{2v}^6) at room temperature and transform to the tetragonal scheelite structure after reaching a critical temperature. The critical temperature depends on the constituent ions in the compositions.¹³ Rooksby *et al.* reported this monoclinic fergusonite structure as a distorted scheelite structure. This distortion was induced by micro strains in the compositions. One of the strains caused the unit cell edges to be unequal, and the other strain caused the deviation of the monoclinic angle from 90° .¹⁴ Therefore, the structure changed from monoclinic fergusonite to tetragonal scheelite. It was predicted that this monoclinic distortion in fergusonite compositions might disappear by supplying sufficient thermal energy and transform to a

Microwave Laboratory, Department of Physics, Indian Institute of Technology Madras, Chennai 600 036, India. E-mail: vrkm@physics.iitm.ac.in

tetragonal scheelite structure.¹³ This type of phase transition was reported by Stubican in rare-earth orthoniobates and tantalates with $A^{3+}B^{5+}O_4$ stoichiometry. The rare-earth tantalates possess a higher transition temperature than the niobates.¹³ Rooksby *et al.* reported that the variation in the nature of the bonding in the NbO_4 and TaO_4 tetrahedron was responsible for the difference in the phase transition temperature. Ta–O bonds are more covalent than Nb–O bonds in these compositions; hence, tantalates require more energy to remove this monoclinic distortion.¹⁴ Therefore, this phase transition temperature was sensitive to the ionic radius of both the rare-earth and B-site cation. This monoclinic \leftrightarrow tetragonal phase transition is second-order and displacive.¹⁵ Errandonea *et al.* reported a pressure-induced scheelite to fergusonite structural transformation in $CaWO_4$ and $SrWO_4$ compositions by using angle dispersive X-ray diffraction and near-edge X-ray absorption studies.¹⁶

The high-temperature tetragonal phase of $LaNbO_4$ was stabilized by replacing Nb^{5+} (0.48 \AA) with lower ionic radius V^{5+} (0.355 \AA).^{17,18} In the same report, the lattice parameters a , c and monoclinic angle β varied with increasing V^{5+} concentration were given. Similar variations in the lattice parameters were reported by Aldred¹⁹ in $CeNbO_4$ and $NdNbO_4$ compositions. The nature of the phase transition in $RENbO_4$ (RE: La, Ce and Nd) was explained by Aldred with Landau theory.¹⁹ One of the most important conclusions from Aldred's study was that V^{5+} substitution in place of Nb^{5+} cannot stabilize the high-temperature tetragonal scheelite structure of $RENbO_4$ compositions with a heavier rare-earth ion at the A-site.¹⁹

This led us to investigate the phase transition mechanism and its stabilization in $SmNbO_4$ composition. To our knowledge, there are no experimental reports of the phase transition mechanism and the composition-induced structural transition in $SmNbO_4$ composition. Therefore, in the present manuscript, we report the nature of the phase transition and stabilization of the high-temperature crystal structure of $SmNbO_4$ with substitution of multiple cations (Si^{4+} and Mo^{6+}) at the Nb site. We report the microwave dielectric properties of both the monoclinic and stabilized tetragonal phases.

2. Experimental procedure

$SmNb_{1-x}(Si_{1/2}Mo_{1/2})_xO_4$ ($x = 0.0\text{--}0.69$) ceramic compositions were synthesized by a conventional solid-state reaction method. Proportionate amounts of the starting materials Sm_2O_3 (99.9%), Nb_2O_5 (99.5%), SiO_2 (99.8%) and MoO_3 (99.95%) were collected in a mortar and ground using a pestle. Both wet and dry mixing procedures were used to achieve homogeneous mixtures. The moisture-sensitive rare-earth oxide, Sm_2O_3 , was pre-heated at 800°C for 10 h before it was weighed at a stoichiometric ratio. All the ground homogeneous mixtures were collected in high-purity alumina crucibles and calcined in the temperature range $1200\text{--}1300^\circ\text{C}$ for 4 h. The agglomerated product obtained from calcination was ground into fine powder by both dry and wet grinding. The phase purity of $SmNb_{1-x}(Si_{1/2}Mo_{1/2})_xO_4$ ($x = 0.0\text{--}0.69$) was studied by collecting

the powder X-ray diffractograms of these compositions by using a Philips PANalytical X'pert Pro X-ray diffractometer with a X'Celerator detector. We used $Cu K_\alpha$ radiation with an accelerating voltage of 40 kV and a current of 30 mA. The incident and receiving Soller slits were maintained at 0.02° , whereas a 1° divergent slit was used for all these measurements. The data was collected with a step of 0.017° . To understand the structural transformation, we performed a Rietveld refinement on all these compositions following the procedure given in the notes of the Canadian Powder Diffraction Workshop.²⁰ The pseudo-Voigt function was used to fit the peak shape by the GSAS suite with EXPGUI software.^{21,22}

Room-temperature Raman spectra of the samples were obtained with a Horiba Jobin Yvon HR800 UV Raman spectrometer equipped with a Peltier-cooled charge-coupled device detector. A He–Ne laser source ($\lambda = 632.8 \text{ nm}$) was used for the measurement and the laser output power was measured as about 3 mW at the sample. The sample was prepared for these measurements by polishing ($0.25 \text{ }\mu\text{m}$ diamond paste) and thermal etching (heated at 500°C for 8 h to remove the strain caused by polishing). The measurement was obtained in the backscattering geometry. An incident slit aperture of $100 \text{ }\mu\text{m}$ and grating of 1800 lines/in. were used to obtain a resolution of 0.3 cm^{-1} . An Olympus BX-41 microscope with a $100\times$ objective lens was used to obtain a laser spot of diameter of about $1 \text{ }\mu\text{m}$ on the sample. The spectrometer was calibrated with a silicon standard prior to the measurement.

The phase stability of $SmNbO_4$ with temperature was probed by differential scanning calorimetry (DSC; SDT Q600, TA Instruments) and temperature variation XRD measurements (PANalytical X'pert Pro X-ray, Philips) equipped with a high-temperature chamber (HTK 16N, Anton Paar). By adding 3 wt% polyvinyl alcohol, pellets of 8 mm in diameter and 7 mm thickness were prepared from these calcined powders. The sintering temperature of these compositions was optimized by using a conventional resistive heating furnace. The Archimedes technique was used for measuring the bulk density of these sintered pellets and it was compared with the theoretical density obtained from the Rietveld refinement. The microwave dielectric properties, such as the dielectric constant (ϵ_r) and quality factor ($Q \times f$), were measured by the Hakki–Coleman method and the reflection cavity technique, respectively. The temperature coefficient of the resonant frequency (τ_f) was measured in the temperature range of $25\text{--}85^\circ\text{C}$ by using an invar cavity attached to a programmable hot plate.

3. Results and discussion

3.1. Temperature-induced phase transition in $SmNbO_4$

Differential scanning calorimetry (DSC) and temperature variation powder X-ray diffraction were used to understand the phase transition mechanism in $SmNbO_4$. In general, DSC is an important tool for identifying structural changes in different classes of materials by measuring the heat flow of corresponding phase transitions. Fig. 1(a) shows the DSC scan of $SmNbO_4$ in the temperature range $100\text{--}1400^\circ\text{C}$. A heating rate of $20^\circ\text{C min}^{-1}$

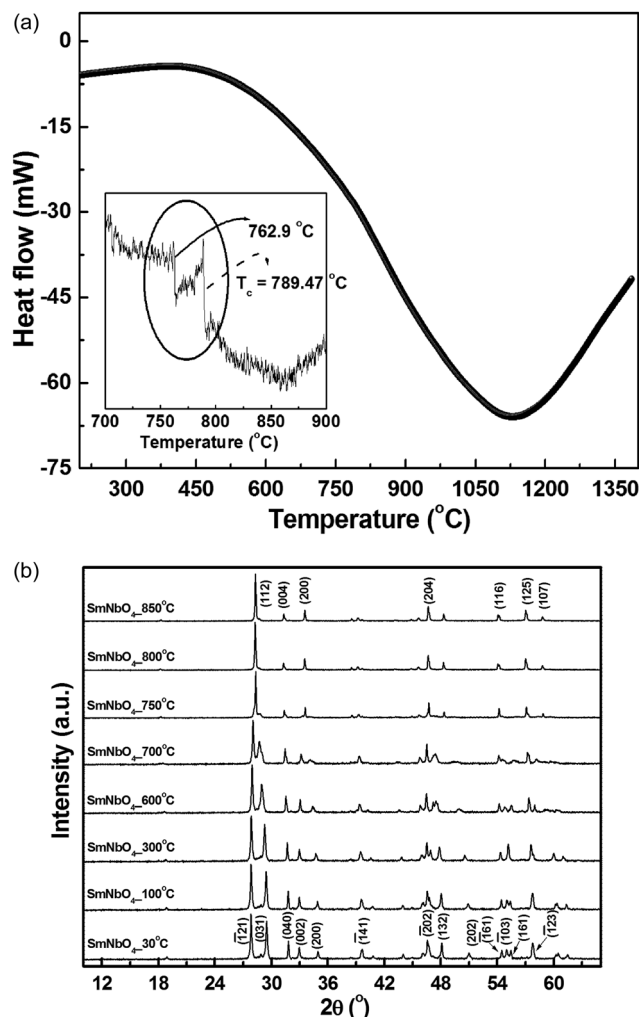


Fig. 1 (a) Differential scanning calorimetry scan of SmNbO₄. (b) Temperature variation of X-ray diffractograms of SmNbO₄.

was used for this measurement. Fig. 1(a) clearly shows a transition starting from 650 to 1130 °C and the transition temperatures of 762 and 789 °C were obtained by differentiating the DSC scan in the range 700–900 °C.

To understand the mechanism of these phase transitions, we performed temperature variation powder X-ray diffraction measurements on SmNbO₄ in the temperature range 30–850 °C (Fig. 1(b)). Rietveld refinement was carried out on all these diffractograms and the compound possessed a monoclinic fergusonite structure at room temperature. Therefore, the room-temperature powder X-ray diffractogram of SmNbO₄ was indexed with monoclinic space group (*I*2/*a*) and JCPDF file no. 32-0496. We observed little variation in the X-ray reflection of SmNbO₄ up to a certain temperature. As the temperature increased further, we observed changes in the X-ray reflections of this compound, possibly caused by the onset of the phase transition. Fig. 1(b) clearly indicates that as the temperature increased, the most intense reflections, (−121) and (031), of room-temperature SmNbO₄ approached each other, whereas the (040) and (002) reflections diverged. Rietveld refinement revealed

that the high-temperature phase of SmNbO₄ was well fitted by the tetragonal scheelite structure with *I*4₁/*a* space group, resulting in satisfactory refinement parameters (*w**R*_p, *R*_p and χ^2). Therefore, the high-temperature powder X-ray diffractogram of SmNbO₄ was indexed with a tetragonal space group. The Rietveld refinement plots of SmNbO₄ at ambient and transition temperatures are shown in Fig. 2(a). The crystal structure of SmNbO₄ at room temperature and high temperature are shown in Fig. 2(a). Crystallographic information, such as space group, atomic positions, bond lengths and occupancies of both the room-temperature and high-temperature phases, are given in Table 1.

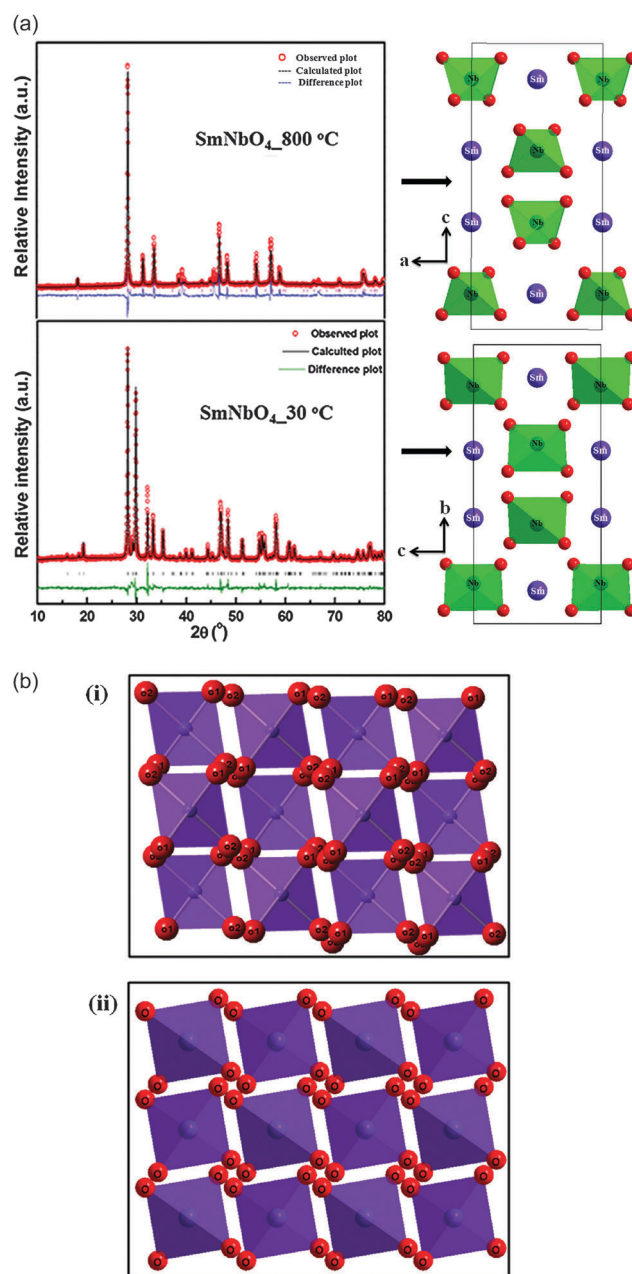


Fig. 2 (a) Rietveld refinement plots and crystal structure of SmNbO₄ at 30 and 800 °C. (b) Tetrahedral arrangement in the (i) room-temperature monoclinic fergusonite and (ii) high-temperature tetragonal scheelite structure.

Table 1 Crystallographic parameters of room-temperature and high-temperature structures of SmNbO_4

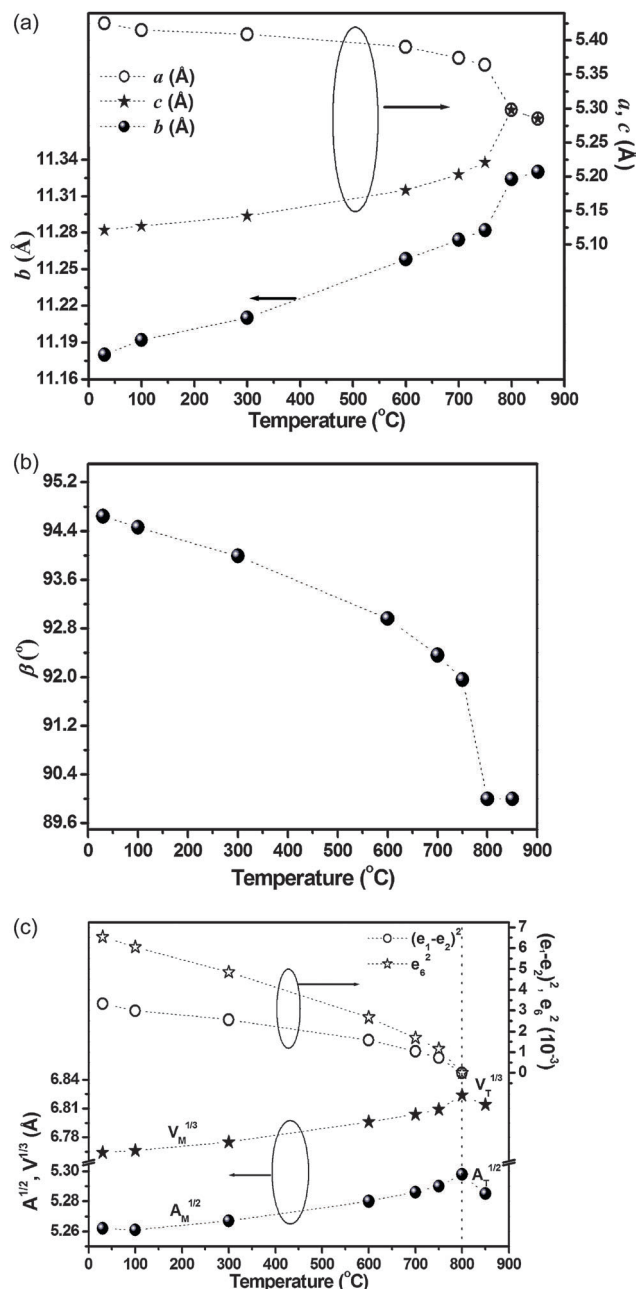
Atom	x	y	z	Occupancy	Bond length (Å)
At 30 °C, space group: $I2/a$					
Sm	0.25	0.619(31)	0	1.0	Sm-O1 ($\times 2$): 2.330
Nb	0.25	0.144(30)	0	1.0	Sm-O2 ($\times 2$): 2.217
O1	0.923(23)	0.953(8)	0.233(24)	1.0	($\times 2$): 2.540
O2	0.468(31)	0.213(8)	0.786(4)	1.0	Nb-O1 ($\times 2$): 1.983
					Nb-O2 ($\times 2$): 1.797
					($\times 2$): 2.338
At 800 °C, space group: $I4_1/a$					
Sm	0	0.25	0.625	1.0	Sm-O ($\times 4$): 2.420
Nb	0	0.25	0.125	1.0	($\times 4$): 2.473
O	0.243(31)	0.078(32)	0.038(12)	1.0	Nb-O ($\times 4$): 1.853

The arrangement of the B-site tetrahedron is an important difference between the room-temperature fergusonite and high-temperature scheelite structure of SmNbO_4 . Fig. 2(b) shows that the B-site tetrahedron is distorted along one of its diagonals in the room-temperature fergusonite structure because of the strains present in SmNbO_4 . However, the symmetrical isolated B-site tetrahedral arrangement is seen in high-temperature scheelite structure because of the decrease in the strains as the temperature increases, and this is confirmed by calculating the spontaneous strain of SmNbO_4 . The fergusonite structure possesses two distinct oxygen positions, O(1) and O(2), whereas the high-temperature scheelite structure of SmNbO_4 contains only one oxygen position in the unit cell. In the high-temperature scheelite structure, the A-site Sm^{3+} cation is connected to eight oxygen atoms, forming a SmO_8 dodecahedron, whereas in the room-temperature SmNbO_4 structure, two oxygen atoms, O(1) and O(2), are connected to the A-site Sm^{3+} cations with two sets of shorter and longer bonds.

The variation in the lattice parameters (a_M , b_M , c_M , a_T and c_T) and β of SmNbO_4 with increasing temperature is shown in Fig. 3(a) and (b) respectively. The suffix M corresponds to the room-temperature monoclinic fergusonite structure, whereas the suffix T corresponds to the tetragonal scheelite structure. Fig. 3(a) shows that as the temperature increases, parameters b_M and c_M increase, whereas a_M and β decrease. On reaching the phase transition temperature (T_0), the lattice parameters, a_M and c_M , that correspond to the monoclinic phase became equal, whereas the monoclinic angle, β , approaches 90° . Therefore, these changes in the lattice parameters result in the decrease of the monoclinic distortion in SmNbO_4 and transform the symmetry of the structure from monoclinic to tetragonal. Table 2 gives the lattice parameters of SmNbO_4 at different temperatures.

Monoclinic distortion in SmNbO_4 arises because of the presence of two homogeneous strains. One of the strains, $(e_1 - e_2)$, transforms the square base of the tetrahedron in the tetragonal structure to a parallelepiped in the monoclinic structure. The other strain, e_6 , makes the angle β deviate from 90° . In this work, we calculated these strains in SmNbO_4 by using the following expressions and the lattice parameters obtained from the Rietveld refinement of temperature variation diffractograms of SmNbO_4 (Table 3).¹⁹

$$(e_1 - e_2) = \frac{(a_M - c_M)}{(a_M c_M)^{1/2}} \quad \text{and} \quad e_6 = \cos(\pi - \beta) \quad (1)$$

**Fig. 3** (a) Temperature variation of a , b and c of SmNbO_4 . (b) Temperature variation of monoclinic angle (β). (c) Temperature variation of strain parameters ($(e_1 - e_2)^2$, e_6^2), volume ($V^{1/3}$) and basal area ($A^{1/2}$).

Here, a_M , c_M and β are the lattice parameters of monoclinic SmNbO_4 , and e_1 , e_2 and e_6 are the elements of the strain tensor.

The variation in both these homogeneous strains with increasing temperature is shown in Fig. 3(c). This clearly shows that both $(e_1 - e_2)$ and e_6 strains decrease with increasing temperature and become zero when the system reaches the transition temperature ($T_0 \sim 800^\circ\text{C}$). The decrease in $(e_1 - e_2)$ is responsible for the lattice parameters a_M and c_M becoming equal, whereas the variation in the monoclinic angle with temperature is attributed to the decrease of e_6 strain in SmNbO_4 . This confirms that the monoclinic distortion vanishes at higher

Table 2 Temperature variation of lattice parameters (*a*, *b*, *c* and β) of SmNbO₄

Temp. (°C)	<i>a</i> (Å)	<i>b</i> (Å)	<i>c</i> (Å)	β (°)	Refinement parameters (<i>wR_p</i> , <i>R_p</i> , χ^2)
30	5.425	11.18	5.121	94.64	8.2%, 9%, 1.98
100	5.415	11.192	5.127	94.46	9.2%, 8.6%, 2.05
300	5.409	11.210	5.142	93.99	8.8%, 9.3%, 2.12
600	5.390	11.258	5.180	92.96	8.3%, 10.2%, 2.23
700	5.374	11.274	5.203	92.36	10.3%, 9.8%, 2.45
750	5.364	11.282	5.221	91.96	9.3%, 10.5%, 2.38
800	5.298	11.324	5.298	90.00	7.8%, 8.7%, 2.05
850	5.285	11.330	5.285	90.00	8.1%, 8.4%, 2.15

Table 3 Temperature variation of strain parameters ($(e_1 - e_2)^2$, e_6^2), basal area ($A^{1/2}$) and volume ($V^{1/3}$) of SmNbO₄

Temp. (°C)	$(e_1 - e_2)^2 \times 10^{-3}$	$e_6^2 \times 10^{-3}$	$A^{1/2}$ (Å)	$V^{1/3}$ (Å)
30	3.326	6.54	5.262	6.764
100	2.98761	6.05	5.261	6.766
300	2.56315	4.84	5.267	6.775
600	1.5795	2.67	5.28	6.796
700	1.04578	1.69	5.286	6.804
750	0.73018	1.16	5.29	6.809
800	0	0	5.298	6.824
850	0	0	5.285	6.814

temperatures. In addition, we calculated the evolution of the basal area of the tetrahedron ($A_M^{1/2}$, $A_T^{1/2}$) and the unit cell volume ($V_M^{1/3}$, $V_T^{1/3}$) with temperature (Fig. 3(c)). The suffixes M and T indicate the monoclinic and tetragonal phases, respectively. This shows a clear discontinuity in volume and basal area at the phase transition temperature ($T_o \sim 800$ °C). The transition temperatures obtained from both DSC and high-temperature powder X-ray diffraction measurements are in good agreement. We observed a slight difference in the transition temperature compared with the theoretical value, which could be attributed to the synthesis conditions.^{23,24} Errandonea *et al.* reported the pressure-driven phase transitions in $A^{2+}\text{WO}_4$ (A: Ca, Sr, Ba, Eu and Pb) and explained the phase transition mechanism with the Landau theory of phase transitions.²⁵ Because there are no experimental reports on the phase transition mechanisms of SmNbO₄ ceramic compositions, we explain this behaviour with the Landau theory of phase transitions.

Two homogeneous strains are responsible for the tetragonal to monoclinic phase transformation, and this leads to the formation of two possible orientation states (S_1 and S_2) in the monoclinic fergusonite structure. These strains affect the crystal symmetry, and hence the changes from $4/m$ to $2/m$. The distortion of each orientation is described with the second-rank strain tensor for monoclinic symmetry, given as²⁵

$$e_{ij}(S_1) = \begin{pmatrix} e_{11} & e_{12} & e_{13} \\ e_{21} & e_{22} & 0 \\ 0 & 0 & e_{33} \end{pmatrix} \quad (2)$$

where S_1 is the one orientation state, and the other orientation state, S_2 , can be obtained from $e_{ij}(S_2) = R e_{ij}(S_1) R^T$, where R and R^T represent the 90° rotation matrix around the monoclinic b -axis and its transpose. The strain components for the present monoclinic to tetragonal transition were calculated using the

lattice parameters obtained from the Rietveld refinement and the following expressions.^{18,26}

$$e_{11} = \frac{c_M \sin \beta_M}{a_T} - 1 \quad (3a)$$

$$e_{22} = \frac{a_M}{a_T} - 1 \quad (3b)$$

$$e_{33} = \frac{b_M}{c_T} - 1 \quad (3c)$$

$$e_{12} = \frac{1}{2} \frac{c_M \cos \beta_M}{a_T} \quad (3d)$$

Here, a_M , b_M , c_M are the lattice parameters corresponding to monoclinic symmetry and a_T , c_T and β_M are those for tetragonal symmetry. Suffixes M and T correspond to monoclinic and tetragonal crystal systems. We calculated both the longitudinal and shear strains by using the following equations derived by Aizu for the monoclinic to tetragonal transition.²⁷

$$e_{ij}^s(S_1) = \begin{pmatrix} -u & v & 0 \\ v & u & 0 \\ 0 & 0 & 0 \end{pmatrix} \quad (4a)$$

$$e_{ij}^s(S_2) = \begin{pmatrix} u & -v & 0 \\ -v & -u & 0 \\ 0 & 0 & 0 \end{pmatrix} \quad (4b)$$

Here, $u = \frac{1}{2}(e_{22} - e_{11})$ is longitudinal strain and $v = e_{12}$ is shear strain.

The scalar spontaneous strain for the monoclinic to tetragonal transition in SmNbO₄ was calculated with increasing temperature by using the following expression, and it is given in Table 4.

$$e_s = \sqrt{u^2 + v^2} \quad (4c)$$

Vullam *et al.* explained the phase transition mechanism in LaNbO₄ with Landau theory and concluded that the transition was second-order in nature and followed a linear relationship between the order parameter (η) and the spontaneous strain (e_s). The order parameter (η) was defined as¹⁵

$$\eta = \left(\frac{T_o - T}{T} \right)^{1/2} \quad \text{and} \quad \eta = k e_s \quad (5)$$

where T_o is the phase transition temperature and k is the correlation number, which is a constant for all the temperatures and specific for a particular system.

Table 4 Spontaneous strain values of SmNbO₄

Temp. (°C)	$u (\times 10^{-2})$	$v (\times 10^{-2})$	$e_s (\times 10^{-2})$
30	3.03	3.91	6.99
100	2.86	3.76	6.68
300	2.63	3.38	6.06
600	2.05	2.52	4.59
700	1.65	2.02	3.69
750	1.38	1.68	3.07
800	0	0	0

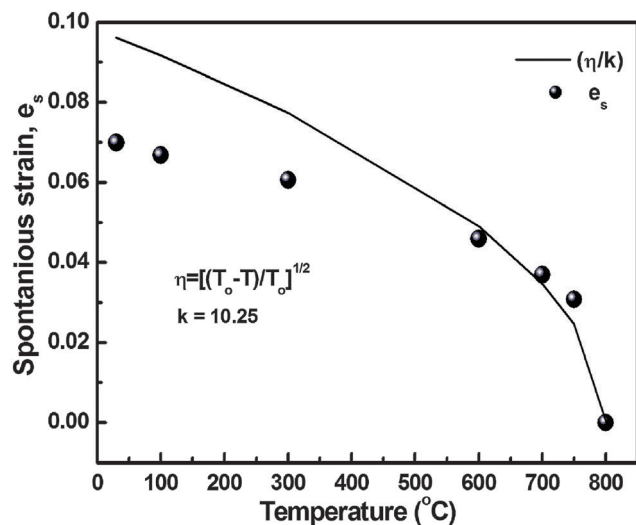


Fig. 4 Relation between spontaneous strain (e_s) and order parameter (η) of SmNbO_4 compound (solid spheres represent e_s values, solid line represents the order parameter).

Fig. 4 shows the relation between the order parameter divided by k (η/k) and the spontaneous strain (solid spheres) values of SmNbO_4 . We optimized the value of k (10.25) to obtain a better fit with the experimental data points. We could not obtain proper fit at lower temperatures, although toward the phase transition temperature, a linear relationship between the order parameter and spontaneous strain values was observed, confirming that the phase transition in SmNbO_4 is second-order.

3.2. Composition-induced structural transformation in SmNbO_4 : X-ray diffraction and Raman spectroscopic studies

Room-temperature X-ray diffractograms of $\text{SmNb}_{1-x}(\text{Si}_{1/2}\text{Mo}_{1/2})_x\text{O}_4$ ($x = 0.0-0.69$) are shown in Fig. 5(a). We performed a Rietveld refinement on all these compositions and observed a monoclinic symmetry in $x < 0.06$ compositions and these diffractograms were indexed with a monoclinic fergusonite structure with $I2/a$ space group. As the concentration of x increased further, the intensity of the reflections (-121) and (031) , corresponding to the monoclinic fergusonite structure, decreased and an additional reflection appeared between these reflections. Rietveld refinement on these compositions revealed that both monoclinic fergusonite and tetragonal scheelite structures coexisted in the $0.06 < x \leq 0.68$ composition range. The $\text{SmNb}_{1-x}(\text{Si}_{1/2}\text{Mo}_{1/2})_x\text{O}_4$ composition with $x = 0.69$ formed a tetragonal scheelite structure with $I4_1/a$ space group, which was the high-temperature crystal structure of SmNbO_4 compositions. Hence, substituting Nb^{5+} with Si^{4+} and Mo^{6+} ions stabilized the high-temperature crystal structure of SmNbO_4 . The crystallographic information, such as atomic positions and occupancies, is given in Table 5, and the corresponding refinement plot is shown in Fig. 5(b).

Fig. 5(c) shows the variation in lattice parameters of $\text{SmNb}_{1-x}(\text{Si}_{1/2}\text{Mo}_{1/2})_x\text{O}_4$ ($x = 0.0-0.69$). In the solid solution region ($x < 0.06$), the lattice parameters did not vary greatly. As the concentration of x increased, the lattice parameters a_M and c_M , corresponding to the monoclinic structure, became equal,

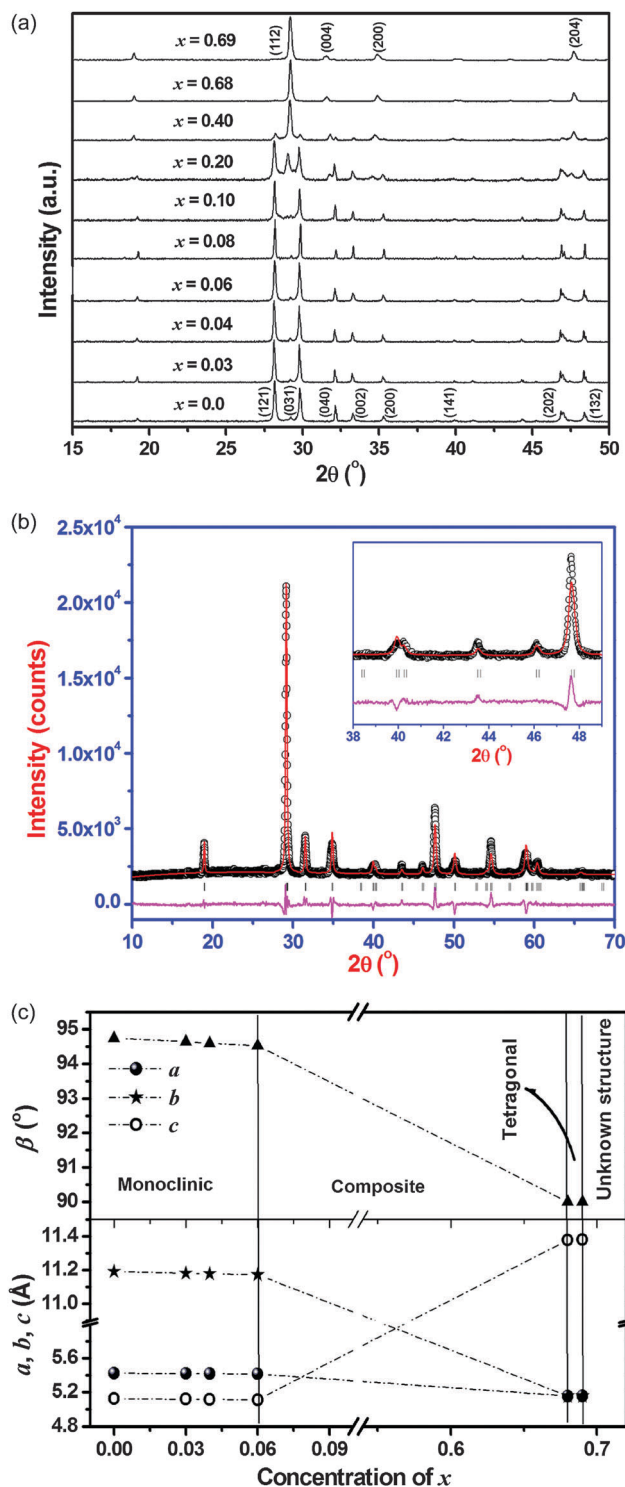


Fig. 5 (a) X-ray diffractograms of $\text{SmNb}_{1-x}(\text{Si}_{1/2}\text{Mo}_{1/2})_x\text{O}_4$. (b) Rietveld refinement plot of $\text{SmNb}_{0.31}(\text{Si}_{1/2}\text{Mo}_{1/2})_{0.69}\text{O}_4$ composition with tetragonal scheelite structure. (c) Variation in lattice parameters of $\text{SmNb}_{1-x}(\text{Si}_{1/2}\text{Mo}_{1/2})_x\text{O}_4$.

whereas the b_M value increased to 11.38 \AA in the tetragonal structure. Similarly, monoclinic angle β decreased from 94.75° to 90° . The different crystallographic phase regions are shown in Fig. 5c, and were similar to earlier reports by Zhou *et al.*^{27,28} In the $\text{ANb}_{1-x}\text{V}_x\text{O}_4$ (A: Ce, Nd; $x = 0.0-1.0$) system, Aldred¹⁹ observed a

Table 5 Wyckoff sites, atomic coordinates, and occupancies of $\text{SmNb}_{0.31-x}(\text{Si}_{1/2}\text{Mo}_{1/2})_{0.69}\text{O}_4$

Atom	Wyckoff site	<i>x</i>	<i>y</i>	<i>z</i>	Occupancy
Sm	4b	0	0.25	0.625	1.0
Nb	4a	0	0.25	0.125	0.31
Si	4a	0	0.25	0.125	0.345
Mo	4a	0	0.25	0.125	0.345
O	16f	0.227(2)	0.081(2)	0.042(7)	1.0

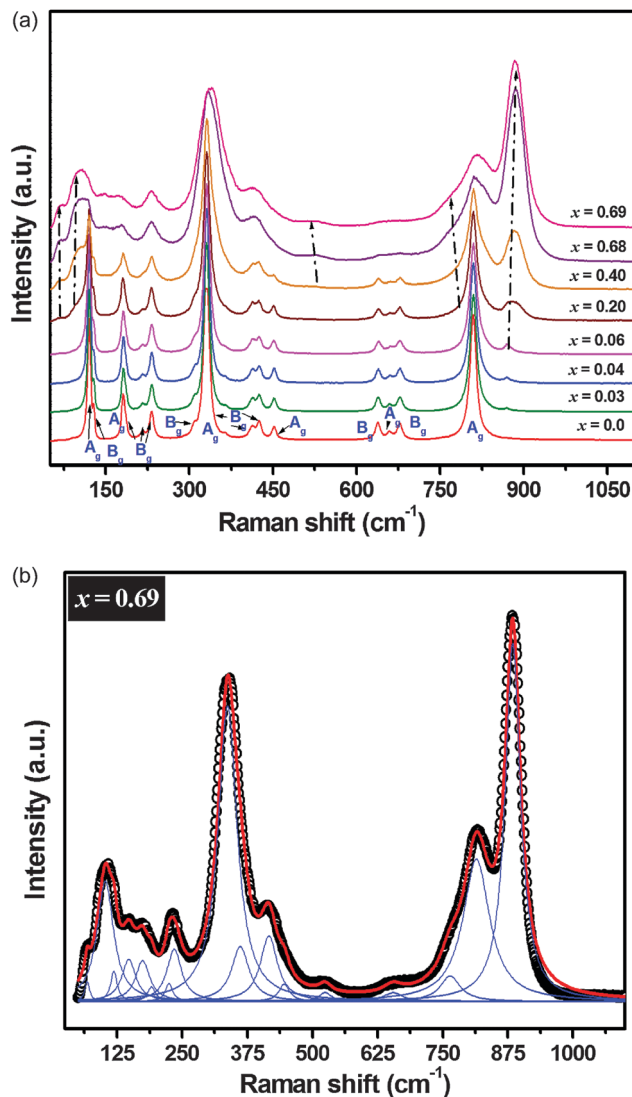
solid solution up to $x \leq 0.30$, where the lattice parameters corresponding to the monoclinic structure became equal, and the b_M value increased. Aldred explained the composition-induced phase transition mechanism in $\text{ANb}_{1-x}\text{V}_x\text{O}_4$ (A: Ce, Nd; $x = 0.0\text{--}1.0$) with Landau theory.¹⁹ The strain parameters were calculated by using the lattice parameters and explained the second-order nature of this phase transition. The formation of a smaller solid solution region ($x < 0.06$) in our present study of $\text{SmNb}_{1-x}(\text{Si}_{1/2}\text{Mo}_{1/2})_x\text{O}_4$ compositions restricted the number of data points (lattice and strain parameters) that could be obtained to understand the exact phase transition mechanism in these compositions. As the lattice parameter variation in $\text{SmNb}_{1-x}(\text{Si}_{1/2}\text{Mo}_{1/2})_x\text{O}_4$ ($x = 0.0\text{--}1.0$) is analogous to the variation in $\text{ANb}_{1-x}\text{V}_x\text{O}_4$ (A: Ce, Nd; $x = 0.0\text{--}1.0$) system reported by Aldred, the decrease in the monoclinic distortion with increasing concentrations of Si^{4+} and Mo^{6+} may be responsible for the monoclinic to tetragonal transition in SmNbO_4 .

Raman spectroscopy is an important spectroscopic technique for understanding the local environment (ordered or disordered), and it provides more information about structural changes in different classes of materials. In the present study, to understand the effect of substitution of Si^{4+} and Mo^{6+} at the Nb^{5+} site of SmNbO_4 on the vibrational characteristics, we performed room-temperature Raman spectroscopic measurements of $\text{SmNb}_{1-x}(\text{Si}_{1/2}\text{Mo}_{1/2})_x\text{O}_4$ ($x = 0.0\text{--}0.69$). Fig. 6 shows the Raman spectra of all these compositions in the range $25\text{--}1100\text{ cm}^{-1}$. Room-temperature SmNbO_4 possesses monoclinic crystal symmetry with $I2/a$ space group. In this structure, both Sm^{3+} and Nb^{5+} cations occupy the 4e Wyckoff site, whereas oxygen anions occupy the 8f site.²⁹ Group theoretical analysis predicts that there are 18 Raman active modes possible for the monoclinic fergusonite structure and the irreducible representation of these modes is given below.^{29,30}

$$\Gamma = 8A_g + 10B_g + 8A_u + 10B_u$$

Here, all the g vibrations are Raman active and all the u modes are IR active.

In the present study, the Raman spectra are in good agreement with earlier reports,²⁹ and all the modes were assigned, as shown in Fig. 6. The Raman modes of the fergusonite structure are grouped into external and internal modes, with RE^{3+} and NbO_4 as two sub-lattices where the modes corresponding to the vibrations of NbO_4 appear on the high wavenumber side because of the covalent nature of the Nb–O bonds. However, all the external modes are present on the low wavenumber side. In the compositions with $x < 0.06$, there was no shift in the Raman modes of SmNbO_4 , whereas an increase in the full

**Fig. 6** (a) Room-temperature Raman spectra of $\text{SmNb}_{1-x}(\text{Si}_{1/2}\text{Mo}_{1/2})_x\text{O}_4$. (b) Deconvoluted Raman spectrum of $\text{SmNb}_{0.31}(\text{Si}_{1/2}\text{Mo}_{1/2})_{0.69}\text{O}_4$ composition.

width at half maximums (FWHMs) of the intense Raman modes (A_g at 808.7 , 331.4 and 120.3 cm^{-1}) was observed. Because the A_g modes arose from the symmetrical stretching vibrations (ν_{sys}) of Nb–O bonds, substitution of Si^{4+} and Mo^{6+} ions at the Nb^{5+} site affected the rigidity of the NbO_4 tetrahedra and this was reflected in the FWHM of the A_g modes.

A new Raman active mode around 868.8 cm^{-1} was observed to start from the $x = 0.06$ composition. Powder X-ray diffraction measurements of $\text{SmNb}_{1-x}(\text{Si}_{1/2}\text{Mo}_{1/2})_x\text{O}_4$ ($x = 0.69$) confirmed that the tetragonal phase started from the $x = 0.06$ composition and the single-phase tetragonal scheelite structure was observed for the $x = 0.69$ composition. With this information, we can confidently assign this new mode at 884.4 cm^{-1} in the $x = 0.69$ composition to the A_g mode, which is the most intense mode corresponding to the symmetric stretching vibrations of (Nb/Si/Mo)–O bonds in the tetragonal scheelite structure. The mode at 814.4 cm^{-1} was assigned to the asymmetric stretching vibrations

of (ν_{asy}) of (Nb/Si/Mo)–O bonds, and the complete assignment of Raman modes for $x = 0.69$ compositions with the tetragonal scheelite structure is shown in Fig. 6(a). Fig. 6(b) shows the deconvoluted Raman spectrum of the $x = 0.69$ composition. The symmetrical stretching vibrational mode corresponding to the tetragonal scheelite structure shifted toward the high wave-number side and can be attributed to the substitution of lower ionic radius Si^{4+} (0.26 Å) and Mo^{6+} (0.41 Å) in place of Nb^{5+} (0.48 Å),¹⁷ which affects the covalence of (Nb/Si/Mo)–O bonds. The low wavenumber Raman modes of $\text{SmNb}_{1-x}(\text{Si}_{1/2}\text{Mo}_{1/2})_x\text{O}_4$ ($x = 0.69$) with a scheelite structure are weak compared with the $x = 0$ composition with a fergusonite structure. The presence of multiple cations at the B-site may be responsible for this behaviour. In the present study, we assigned some of the Raman modes of $\text{SmNb}_{0.31}(\text{Si}_{1/2}\text{Mo}_{1/2})_{0.69}\text{O}_4$ with a tetragonal scheelite structure (Table 6). Along with powder X-ray diffraction analysis, this systematic variation in the Raman spectra of $\text{SmNb}_{1-x}(\text{Si}_{1/2}\text{Mo}_{1/2})_x\text{O}_4$ ($x = 0.0$ –0.69) confirms the transformation of the monoclinic fergusonite to the tetragonal scheelite structure with the substitution of Nb^{5+} with Si^{4+} and Mo^{6+} .

Because this phase transition temperature is sensitive to the ionic radius of the constituent elements, to observe the effect of substitution of Si^{4+} and Mo^{6+} at the Nb site of SmNbO_4 , we performed DSC measurements on $\text{SmNb}_{1-x}(\text{Si}_{1/2}\text{Mo}_{1/2})_x\text{O}_4$ ($x = 0.0, 0.03, 0.04$). Fig. 7 shows the DSC scans of these compositions, and clearly shows that the phase transition temperature (T_0) increased slightly with increasing x . The substitution of the smaller ionic radius elements (Si^{4+} and Mo^{6+}) for the larger ionic radius element (Nb^{5+}) increases the covalence of the corresponding bonds and requires a higher energy to remove the monoclinic distortion in these compositions. Hence, the variation in the covalence may be responsible for the increase in this phase transition temperature. The increase in the phase transition temperature is smaller because of the substitution of Nb^{5+} with lower concentrations of Si^{4+} and Mo^{6+} . These DSC measurements reveal that the unknown phase transition around 760 °C is suppressed with increasing the concentration of x . The exact reason for the suppression of this unknown phase transition is unclear.

Table 6 Raman mode assignment for $\text{SmNb}_{0.31}(\text{Si}_{1/2}\text{Mo}_{1/2})_{0.69}\text{O}_4$

Mode	Wavenumber (cm^{-1})
A_g	884.4
B_g	814.4
E_g	765.7
—	657.4
—	524.1
B_g	446.6
A_g	415.8
E_g	362.9
A_g	337.0
B_g	233.0
—	216.6
—	176.6
—	146.1
E_g	117.1
B_g	100.0
—	67.60

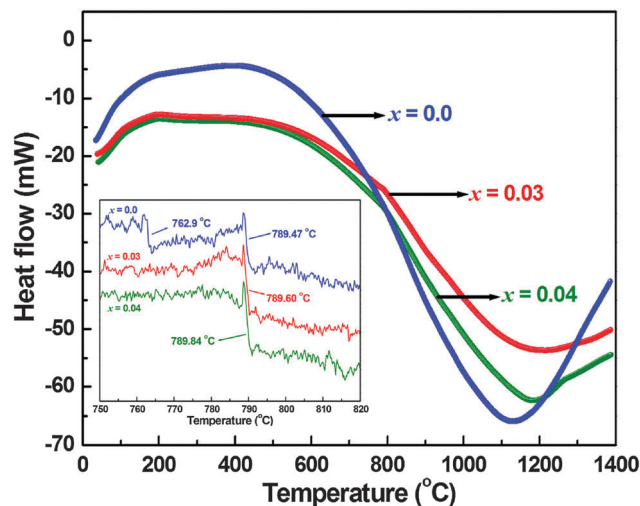


Fig. 7 Differential scanning calorimetry scan of $\text{SmNb}_{1-x}(\text{Si}_{1/2}\text{Mo}_{1/2})_x\text{O}_4$.

4. Density and microstructural studies

The Archimedes principle was used to measure the bulk density of sintered pellets of $\text{SmNb}_{1-x}(\text{Si}_{1/2}\text{Mo}_{1/2})_x\text{O}_4$ ($x = 0.0$ –0.69). The percentage density was calculated by using both the measured and theoretical density of the compositions. The theoretical density of all these compositions was calculated with the following formula.³¹

$$\rho_{\text{th}} = \frac{nM}{NV} \text{ g cm}^{-3} \quad (6)$$

Here, n and M represent the number of formula units per unit cell, which can be obtained from the crystal structure of the composition and molecular weight. N is Avogadro's number ($6.022 \times 10^{23} \text{ mol}^{-1}$) and V is the molar volume of the corresponding composition, and is calculated with the lattice parameters obtained from Rietveld refinement. The percentage of the theoretical density of all these compositions was calculated by using the following equation.

$$\rho(\%) = \frac{\rho_{\text{m}}}{\rho_{\text{th}}} \times 100$$

Here, ρ_{m} is the measured density and ρ_{th} is the theoretical density.

All $\text{SmNb}_{1-x}(\text{Si}_{1/2}\text{Mo}_{1/2})_x\text{O}_4$ ($x = 0.0$ –0.69) had a theoretical density of more than 95%. Scanning electron microscopy (Quanta 400, FEI) studies on polished and thermally etched compositions showed that the microstructures are well compacted and exhibited little variation in grain size with substitution of Nb^{5+} by Si^{4+} and Mo^{6+} (Fig. 8).

5. Microwave dielectric studies of $\text{SmNb}_{1-x}(\text{Si}_{1/2}\text{Mo}_{1/2})_x\text{O}_4$ ($x = 0.0, 0.03, 0.04, 0.68$ and 0.69)

The microwave dielectric properties of $\text{SmNb}_{1-x}(\text{Si}_{1/2}\text{Mo}_{1/2})_x\text{O}_4$ ($x = 0.0, 0.03, 0.04, 0.68$ and 0.69) ceramic compositions, such

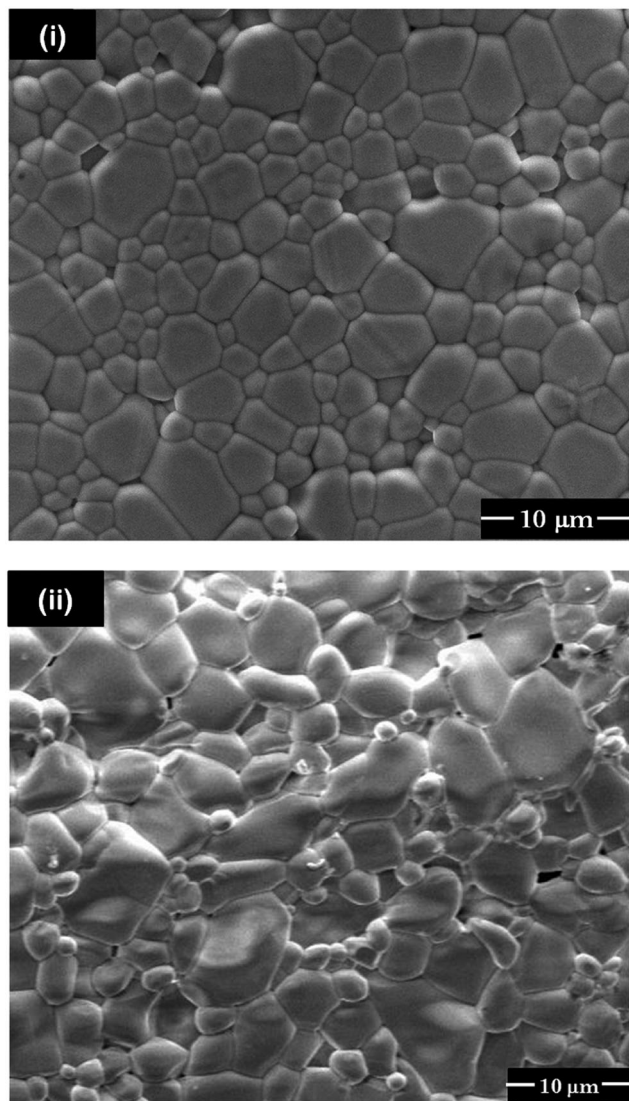


Fig. 8 Surface morphology of $\text{SmNb}_{1-x}(\text{Si}_{1/2}\text{Mo}_{1/2})_x\text{O}_4$ (i) SmNbO_4 sintered at $1300\text{ }^\circ\text{C}$ (ii) $\text{SmNb}_{0.31}(\text{Si}_{1/2}\text{Mo}_{1/2})_{0.69}\text{O}_4$ sintered at $1350\text{ }^\circ\text{C}$.

as dielectric constant and quality factor, were measured by using Hakki–Coleman and reflection cavity techniques, respectively. The temperature coefficient of the resonant frequency of these compositions was measured with an invar cavity attached to a programmable hot plate. The microwave dielectric properties of all these compositions are given in Table 7.

The variation in the dielectric constant of $\text{SmNb}_{1-x}(\text{Si}_{1/2}\text{Mo}_{1/2})_x\text{O}_4$ ($x = 0.0, 0.03, 0.04, 0.68$ and 0.69) is shown in Fig. 9. In general, the dielectric constant of ceramic materials depends on the extrinsic parameters, such as porosity and secondary phases, and intrinsic parameters, such as polarizability and structural characteristics, of the materials.^{32–34} In our present study, $\text{SmNb}_{1-x}(\text{Si}_{1/2}\text{Mo}_{1/2})_x\text{O}_4$ ($x = 0.0, 0.03, 0.04, 0.68$ and 0.69) had a theoretical density of more than 95%, and hence the effect of porosity on the dielectric constant of these materials was negligible. Choi *et al.* reported that the dielectric constant of ceramic materials at microwave frequencies depends on the

Table 7 Lattice parameters, percentage of theoretical density ($\rho\%$) and microwave dielectric properties (dielectric constant (ϵ_r), quality factor ($Q \times f$) and temperature coefficient of resonant frequency (τ_f)) of $\text{SmNb}_{1-x}(\text{Si}_{1/2}\text{Mo}_{1/2})_x\text{O}_4$

x	a (Å)	b (Å)	c (Å)	β (°)	ρ (%)	ϵ_r	$(Q \times f)$ (GHz)	τ_f (ppm $^\circ\text{C}^{-1}$)
0.0	5.425	11.192	5.127	94.75	95.6	17.3	48 200	−47.3
0.03	5.423	11.182	5.122	94.65	94.7	17.1	46 150	−46.1
0.04	5.420	11.178	5.120	94.60	94.2	16.8	45 300	−45.6
0.68	5.157	5.157	11.378	90	95.4	15.9	33 400	−39.6
0.69	5.158	5.158	11.38	90	93.8	15.6	32 800	−38.2

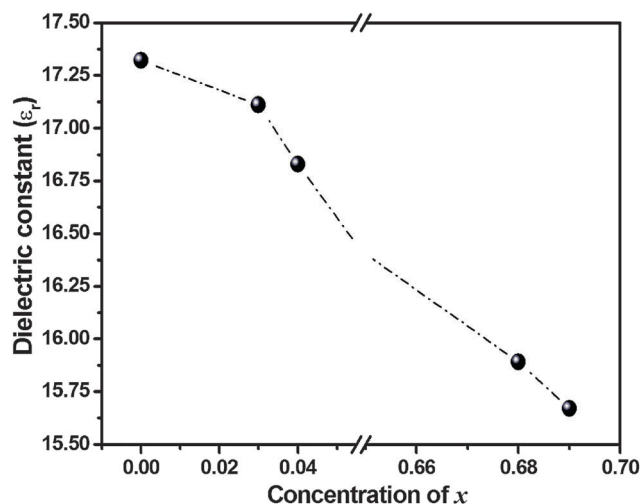


Fig. 9 Variation in dielectric constant of $\text{SmNb}_{1-x}(\text{Si}_{1/2}\text{Mo}_{1/2})_x\text{O}_4$.

ionic polarizability of the constituent ions.³⁵ Similarly, Kim *et al.* explained the higher dielectric constant of lead-based scheelite structured materials than ABO_4 (A: Ca, Ba; B: Mo, W) compounds by the higher ionic polarizability of lead compared with other ions.³⁶ In this study, the dielectric constant decreased with increasing x . It has been reported that Si^{4+} (0.87 \AA^3) and Mo^{6+} (3.60 \AA^3) possess a lower polarizability than Nb^{5+} (3.97 \AA^3).³⁷ Therefore, increasing the concentration of x replaces the more polarizable Nb^{5+} (3.97 \AA^3) ions with less polarizable Si^{4+} (0.87 \AA^3) and Mo^{6+} (3.60 \AA^3) ions. Hence, the decrease in the dielectric constant of $\text{SmNb}_{1-x}(\text{Si}_{1/2}\text{Mo}_{1/2})_x\text{O}_4$ ($x = 0.0, 0.03, 0.04, 0.68$ and 0.69) is explained by the lower polarizability of the Si^{4+} (0.87 \AA^3) and Mo^{6+} (3.60 \AA^3) ions.

The quality factor of $\text{SmNb}_{1-x}(\text{Si}_{1/2}\text{Mo}_{1/2})_x\text{O}_4$ ($x = 0.0, 0.03, 0.04, 0.68$ and 0.69) was measured by using the reflection cavity technique and are given in Table 7. Fig. 10 shows the quality factor variation with increasing x . The pure rare-earth orthoniobate compound (SmNbO_4 : 48 200 GHz) with a monoclinic fergusonite structure possessed a higher quality factor than the stabilized ($x = 0.69$: 32 800 GHz) composition with the tetragonal scheelite structure. The quality factor of ceramic materials at microwave frequencies depends on processing parameters such as density, porosity, secondary phases and grain growth.^{38,39} Surendran *et al.* reported the dependence of the quality factor on the structural transitions in microwave

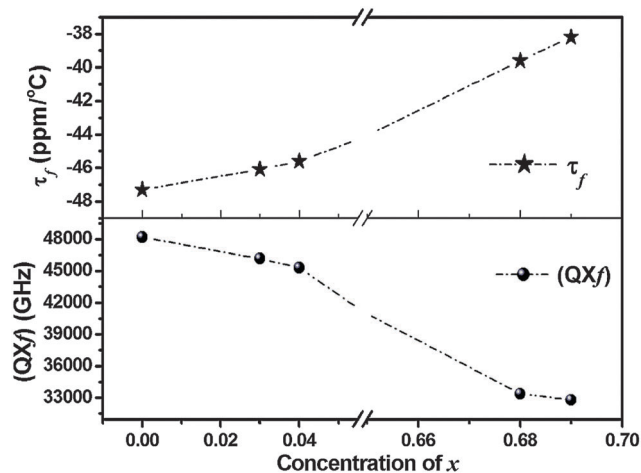


Fig. 10 Variation in quality factor and temperature coefficient of resonant frequency of $\text{SmNb}_{1-x}(\text{Si}_{1/2}\text{Mo}_{1/2})_x\text{O}_4$.

dielectric materials where they observed a decrease in quality factor when approaching the phase transition region.⁴⁰ Solomon *et al.* explained the decrease in quality factor with a phase transition mechanism.⁴¹ In our study of $\text{SmNb}_{1-x}(\text{Si}_{1/2}\text{Mo}_{1/2})_x\text{O}_4$, from $x = 0.0$ to 0.69 , the structure continuously changed from the monoclinic to tetragonal structure, which was confirmed by the X-ray and Raman spectroscopic measurements. This onset of structural change may be responsible for the systematic decrease in the quality factor in Fig. 10.

Fig. 10 shows the variation in temperature coefficient of the resonant frequency (τ_f) of $\text{SmNb}_{1-x}(\text{Si}_{1/2}\text{Mo}_{1/2})_x\text{O}_4$ ($x = 0.0, 0.03, 0.04, 0.68$ and 0.69) ceramic compositions. τ_f changed from $-47 \text{ ppm } ^\circ\text{C}^{-1}$ for $x = 0.0$ to $-38 \text{ ppm } ^\circ\text{C}^{-1}$ for $x = 0.69$ composition in moving from Nb^{5+} -rich to Nb^{5+} -poor compositions. Therefore, we observed a slight improvement in τ_f and it shifted toward zero when the systems approached the phase transition region, which is consistent with earlier reports of microwave dielectric materials where they reported that the temperature coefficient of the resonant frequency (τ_f) had minimum values when the system approached the phase transition region.⁴²

6. Conclusions

All the $\text{SmNb}_{1-x}(\text{Si}_{1/2}\text{Mo}_{1/2})_x\text{O}_4$ ($x = 0.0-0.69$) compositions were synthesized by the solid-state reaction method. Temperature variation X-ray diffraction measurements revealed that pure rare-earth orthoniobate (SmNbO_4) possessed a monoclinic fergusonite structure with $I2/a$ space group at room temperature and transformed to a tetragonal scheelite structure with $I4_1/a$ space group around 800°C . This transition was explained with Landau theory. Both room-temperature powder X-ray diffraction and Raman spectroscopic measurements of $\text{SmNb}_{1-x}(\text{Si}_{1/2}\text{Mo}_{1/2})_x\text{O}_4$ compositions revealed that the crystal system moved from the monoclinic to tetragonal system with increasing x . Rietveld refinement revealed that $\text{SmNb}_{1-x}(\text{Si}_{1/2}\text{Mo}_{1/2})_x\text{O}_4$ formed a solid solution up to $x < 0.06$ with a monoclinic fergusonite structure,

whereas the composition $x = 0.69$ formed in the tetragonal scheelite structure. Both the monoclinic and tetragonal phases coexisted in the range of $0.06 < x \leq 0.68$ and similar variation was observed in the Raman spectroscopy measurements. An unknown transition around 760°C was suppressed by substitution of Nb^{5+} with Si^{4+} and Mo^{5+} . Moreover, a slight increase in the phase transition temperature (T_0) was observed as concentration of x increased from 0.0 to 0.04 . Both the monoclinic and stabilized tetragonal phases possessed good microwave dielectric properties.

Acknowledgements

Author S. D. Ramarao thanks University Grants Commission, Delhi, India and Indian Institute of Technology Madras for providing fellowship in the form of Senior Research Fellowship.

References

- 1 I. A. Kamenskikh, V. N. Kolobanova, V. V. Mikhailina, L. I. Potkin, I. N. Shpinkova, D. A. Spasskya, B. I. Zadneprovskiy and G. Zimmerer, *Nucl. Instrum. Methods Phys. Res., Sect. A*, 2001, **470**, 270.
- 2 L. Hoffart, U. Heider, L. Jorissen, R. A. Huggins and W. Witschel, *Ionics*, 1995, **1**, 131.
- 3 B. Yan and J. H. Wu, *Mater. Chem. Phys.*, 2009, **116**, 67.
- 4 H. Shi, X. L. Huang, H. Tian, J. Lv, Z. Li, J. Ye and Z. Zou, *J. Phys. D: Appl. Phys.*, 2009, **42**, 125402.
- 5 D. A. Pinnow, L. G. Van Uitert, A. W. Warner and W. A. Bonner, *Appl. Phys. Lett.*, 1968, **15**, 83.
- 6 K. S. Vorres, *J. Chem. Educ.*, 1962, **39**, 566.
- 7 S. H. Yoon, D. W. Kim, S. Y. Cho and K. S. Hong, *J. Eur. Ceram. Soc.*, 2006, **26**, 2051.
- 8 R. C. Pullar, S. Farrah and N. M. Alford, *J. Eur. Ceram. Soc.*, 2007, **27**, 1059.
- 9 E. S. Kim, B. S. Chun, R. Freer and R. J. Cernik, *J. Eur. Ceram. Soc.*, 2010, **30**, 1731.
- 10 G. K. Choi, J. R. Kim, S. H. Yoon and K. S. Hong, *J. Eur. Ceram. Soc.*, 2007, **27**, 3063.
- 11 D. Zhou, L.-X. Pang and Z.-M. Qi, *Inorg. Chem.*, 2014, **53**, 9222.
- 12 R. C. Ewing, *Am. Mineral.*, 1975, **60**, 728.
- 13 V. S. Stubican, *J. Am. Ceram. Soc.*, 1964, **47**, 55.
- 14 H. P. Rooksby and E. A. D. White, *Acta Crystallogr.*, 1963, **16**, 888.
- 15 F. Vullum, F. Nitsche, S. M. Selbach and T. Grande, *J. Solid State Chem.*, 2008, **181**, 2580.
- 16 D. Errandonea, J. P. Porres, F. J. Manjon, A. Segura, Ch. F. Roca, R. S. Kumar, O. Tschauner, P. R. Hernandez, J. L. Solano, S. Radescu, A. Mujica, A. Munoz and G. Aquilanti, *Phys. Rev. B: Condens. Matter Mater. Phys.*, 2005, **72**, 174106.
- 17 R. D. Shannon, *Acta Crystallogr., Sect. A: Cryst. Phys., Diffraction, Theor. Gen. Crystallogr.*, 1976, **32**, 751.
- 18 A. T. Aldred, *Mater. Lett.*, 1983, **1**, 197.
- 19 A. T. Aldred, *J. Solid State Chem.*, 1985, **59**, 95.

- 20 L. Cranswick and I. Swainson, 7th Canadian Powder workshop notes: <http://www.cins.ca/cpdw/notes.html>. 2007.
- 21 A. C. Larson and R. B. von Dreele, *General Structural Analysis System (GSAS)*, Los Alamos National Laboratories, Los Alamos, NM, 1990.
- 22 B. H. Toby, *J. Appl. Crystallogr.*, 2001, **34**, 210.
- 23 E. K. Salje, *Phase Transitions in Ferroelastic and Co-elastic Crystals*, Cambridge University Press, 1991.
- 24 K. Ishikawa, K. Yoshikawa and N. Okada, *Phys. Rev. B: Condens. Matter Mater. Phys.*, 1988, **37**, 5852.
- 25 D. Errandonea, *Europhys. Lett.*, 2001, **77**, 56001-P1.
- 26 J. L. Schlenker, G. V. Gibbs and M. B. Boisen, *Acta Crystallogr., Sect. A: Cryst. Phys., Diffraction, Theor. Gen. Crystallogr.*, 1978, **34**, 52.
- 27 D. Zhou, L.-X. Pang, J. Guo, Z.-M. Qi, T. Shao, X. Yao and C. A. Randall, *J. Mater. Chem.*, 2012, **22**, 21412.
- 28 D. Zhou, W.-B. Li, L.-X. Pang, J. Guo, Z.-M. Qi, T. Shao, X. Yao and C. A. Randall, *Dalton Trans.*, 2014, **43**, 7290.
- 29 K. Aizu, *J. Phys. Soc. Jpn.*, 1970, **28**, 706.
- 30 K. P. F. Siqueira, L. R. Moreira and A. Dias, *Chem. Mater.*, 2010, **22**, 2668.
- 31 D. L. Rousseau, R. P. Bauman and S. P. S. Porto, *J. Raman Spectrosc.*, 1981, **10**, 253.
- 32 Q. Liao, L. Li, X. Ren and X. Ding, *J. Am. Ceram. Soc.*, 2011, **94**, 3237.
- 33 S. J. Penn, N. Mc N. Alford, A. Templeton, X. Wang, M. Xu, M. Reece and K. J. Scherapell, *J. Am. Ceram. Soc.*, 1997, **80**, 1885.
- 34 W. S. Kim, E. S. Kim and K. H. Yoon, *J. Am. Ceram. Soc.*, 1999, **82**, 2111.
- 35 A. Dias, G. Subodh, M. T. Sebastian, M. M. Lage and R. L. Moreira, *Chem. Mater.*, 2008, **20**, 4347.
- 36 G. K. Choi, J. R. Kim, S. H. Yoon and K. S. Hong, *J. Eur. Ceram. Soc.*, 2007, **27**, 3063.
- 37 E. S. Kim, B. S. Chun, R. Freer and R. J. Cernik, *J. Eur. Ceram. Soc.*, 2010, **30**, 1731.
- 38 R. D. Shannon, *J. Appl. Phys.*, 1993, **73**, 348.
- 39 M. H. Liang, C. T. Hu, H. F. Cheng, I. N. Lin and J. J. Steeds, *J. Eur. Ceram. Soc.*, 2001, **21**, 2759.
- 40 W. S. Kim, E. S. Kim and K. H. Yoon, *J. Am. Ceram. Soc.*, 1999, **82**, 2111.
- 41 K. P. Surendran, P. Mohanan and M. T. Sebastian, *J. Eur. Ceram. Soc.*, 2003, **23**, 2489.
- 42 S. Solomon, M. Kumar, K. P. Surendran, M. T. Sebastian and P. Mohanan, *Mater. Chem. Phys.*, 2001, **67**, 291.